NOAA Technical Memorandum ERL WMPO-11

U.S. DEPARTMENT OF COMMERCE
NATIONAL OCEANIC AND ATMOSPHERIC ADMINISTRATION
Environmental Research Laboratories

Numerical Gravity Wave and Linear Advection Experiments on a One-Dimensional Nested Grid

MICHAEL S. MOSS

Weather Modification Program Office
BOULDER, COLORADO
January 1974

NHRL-107

ONMENTAL RESEARCH LABORATORIES

THER MODIFICATION PROGRAM OFFICE

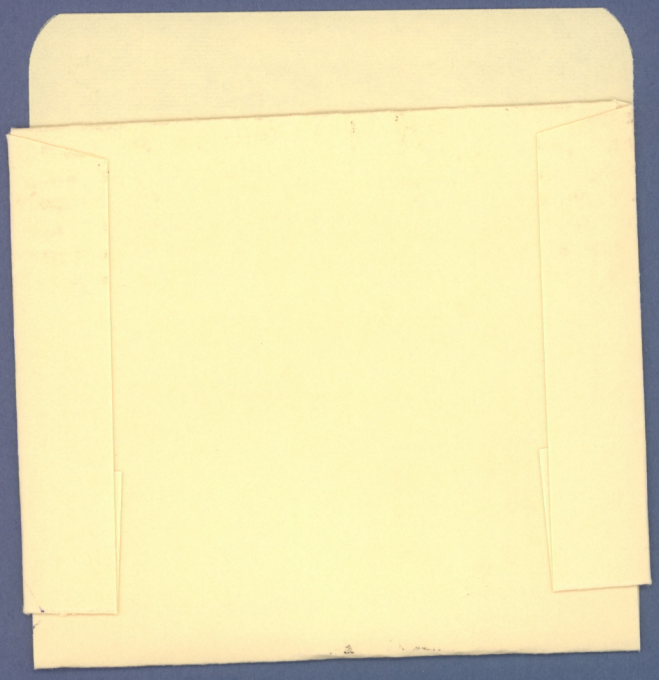

IMPORTANT NOTICE

Technical Memoranda are used to insure prompt dissemination of special studies which, though of interest to the scientific community, may not be ready for formal publication. Since these papers may later be published in a modified form to include more recent information or research results, abstracting, citing, or reproducing this paper in the open literature is not encouraged. Contact the author for additional information on the subject matter discussed in this Memorandum.

NATIONAL OCEANIC AND ATMOSPHERIC ADMINISTRATION

U.S. DEPARTMENT OF COMMERCE
National Oceanic and Atmospheric Administration
Environmental Research Laboratories

NOAA Technical Memorandum ERL WMPO-11

NUMERICAL GRAVITY WAVE AND LINEAR ADVECTION EXPERIMENTS ON A ONE-DIMENSIONAL NESTED GRID

Michael S. Moss
National Hurricane Research Laboratory

Weather Modification Program Office
Boulder, Colorado
January 1974

Contents

NUMERICAL GRAVITY WAVE AND LINEAR ADVECTION EXPERIMENTS ON A ONE-DIMENSIONAL NESTED GRID

Michael S. Moss

Numerical experiments with a mesh refinement technique are applied to the finite difference equations that represent one-dimensional gravity wave and advection phenomena. The grid consists of a coarse mesh and a fine mesh interfaced at the origin. The problem of a nearly monochromatic sine wave approaching the interface from the fine-mesh side is examined. Numerical experiments that parallel the analytic study of Morse (1973) confirm most of his conclusions. In addition, there is a relatively short wave cutoff, below which practically all the energy is trapped on the fine mesh. Integrating a linear advection equation on the nested grid results in a $2\Delta x$ separation of the solution on the fine mesh after the wave reaches the interface. The problem is corrected by using upstream differences for evaluating the tendency at the interface.

1. INTRODUCTION

Recently Moss and Jones (1973) discussed the results of experiments that incorporated a one-dimensional nested grid. In these experiments, the nested grid consisted of a fine mesh (30 km grid increment) centered on a coarse mesh (90 km grid increment). The Matsuno (1966) time integration procedure was applied to a perturbation initially centered on both grids. Unfortunately, the events that occurred when the perturbation crossed the interface of the grids were obscured by computational dispersion and the tendency of the integration scheme to damp high-frequency gravity waves.

In this paper, results of experiments using "neutral" integration procedures applied to nearly monochromatic waves are presented. The first part of this paper discusses results from numerical

experiments comparable with those of Morse (1973). He obtained an analytic solution to the one-dimensional wave equation on a nested grid. In the second part of this paper, results from various nested-grid linear advection experiments are presented.

2. MODEL EQUATIONS AND THE NESTED GRID

The partial differential equations used in this study are as follows. For the gravity wave,

$$\frac{\partial}{\partial t} p^*u = - R\overline{T} \frac{\partial p^*}{\partial x} , \tag{1}$$

$$\frac{\partial}{\partial t} p^* = - \frac{\partial}{\partial x} p^*u , \tag{2}$$

and the linear advection equation is given by

$$\frac{\partial}{\partial t} p^* = - \overline{u} \frac{\partial}{\partial x} p^* . \tag{3}$$

A derivation of equations similar to these is given by Moss and Jones (1973).

The symbols are defined as follows:

t - time,

x - east-west direction,

u - east-west velocity component,

p* - surface pressure,

R - specific gas constant for dry air,

$\overline{T}$ - mean temperature (300° K), and

$\overline{u}$ - constant advecting current.

The spatial domain is represented by two, mutually interacting, 96 or 97 point, uniform grids, each having a different mesh length. In most of the experiments, the ratio of the mesh lengths is 3:1 (see fig. 1); in which case the fine mesh coincides with the right one-third of a coarse mesh. This grid-mesh ratio is the same as that used in the National Hurricane Research Laboratory (NHRL), three-dimensional, nested-grid hurricane model (Jones, 1974). For the other experiments, the ratio is 2:1, and the fine mesh coincides with the right half of the coarse mesh. The remaining discussion in this section refers to experiments with a 3:1 grid-mesh ratio.

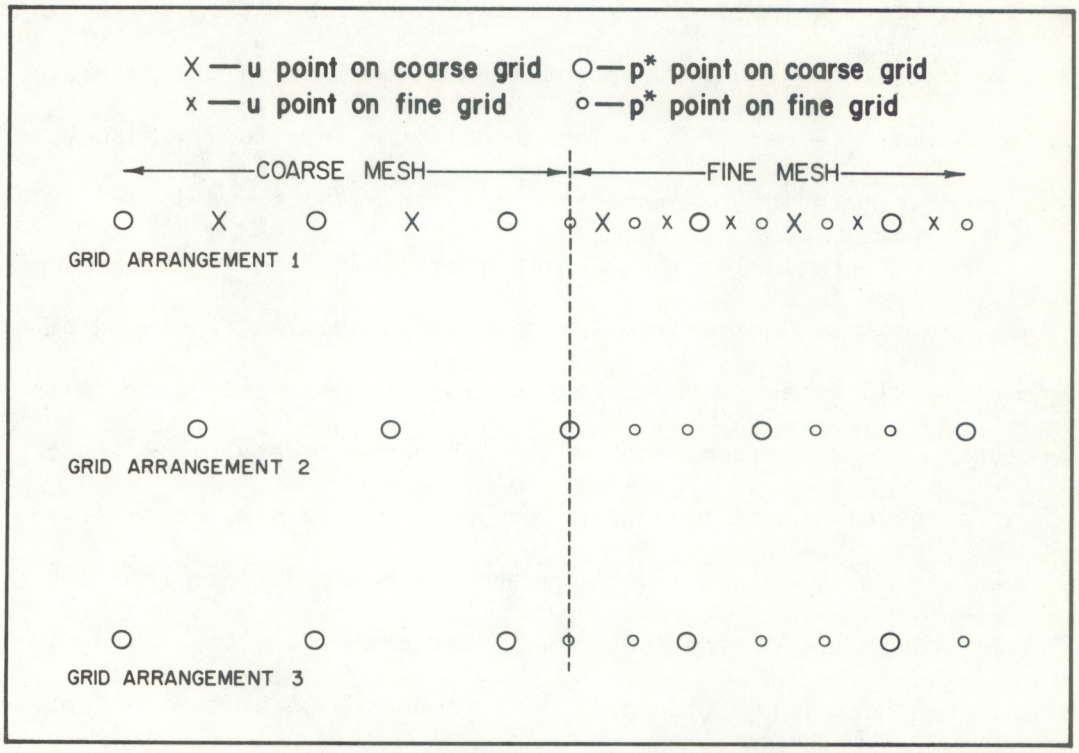

Figure 1. Sample data arrangements for various experimental grids (3:1 grid-mesh ratio). Vertical dashed line represents the mesh interface.

In the gravity-wave experiments, the two dependent variables (p*u and p*) are staggered in space. An example of this grid arrangement is presented at the top of figure 1. In the advection experiments, two different grid arrangements were used (see bottom of fig. 1). When coarse-grid points coincide with the mesh interface (grid arrangement 2), the fine mesh tendency there is simply assigned the value of the coinciding coarse-mesh point. When coarse-grid points do not coincide with the interface (grid arrangement 3) the interface tendency is obtained by a linear interpolation of the coarse-grid tendency just outside the interface and the fine-grid tendency one fine-grid interval inside the interface. The computation of the interface tendencies on grid arrangement 1 is a combination of the above two techniques. A detailed explanation of the interface tendency calculations for grid arrangement 1 is given by Moss and Jones (1973).

The integration of the equations proceeds from the coarse mesh to the fine mesh. Coarse-grid variables that overlap fine-grid points are reevaluated by applying a Schuman (1957) type three-point filtering operator to the coincident and adjacent fine-mesh data. The fine-mesh grid increment and time step are 30 km and 40 sec, respectively. The coarse-grid space and time increments are appropriate integer multiples of those for the fine mesh. For example, with a 3:1 grid-mesh ratio, the coarse-grid spatial increment is 90 km and the coarse-grid time step is 2 min. Some experiments had the time step the same on both grids.

3. GRAVITY WAVE EXPERIMENTS

Following Morse (1973), the integration scheme used for the gravity wave (GW) experiments is

$$p^*u_j^{n+1} = p^*u_j^n - R\bar{T}\,(p^*_{j+\frac{1}{2}}^{\,n} - p^*_{j-\frac{1}{2}}^{\,n})\,\frac{\Delta t}{\Delta x} \qquad (4)$$

$$p^*_{j-\frac{1}{2}}^{\,n+1} = p^*_{j-\frac{1}{2}}^{\,n} - (p^*u_j^{n+1} - p^*u_{j-1}^{n+1})\,\frac{\Delta t}{\Delta x}\ , \qquad (5)$$

where the subscripts denote relative spatial locations and the superscripts are the time levels. The norm of the amplification matrix for the finite difference equations (4) and (5) is unity for $c\,\frac{\Delta t}{\Delta x} < 1$ (Richtmyer and Morton, 1967); therefore, the scheme is neutral when this condition is satisfied. The propagation speed (c) is obtained from (1) and (2) and is

$$c = \pm\sqrt{R\bar{T}}\ . \qquad (6)$$

The initial conditions are

$$p^*\,(x, t = 0) = \bar{p} = 103\ cb$$

$$p^*u\,(x, t = 0) = 0\ . \qquad (7)$$

The lateral boundary conditions are specified by

$$p^*\,(x=0_{coarse},\ t) = \bar{p}\ , \qquad (8)$$

and

$$p^*\,(x=jmax\Delta x_{fine},\ t) = \bar{p} + \sin\,(\frac{2\pi}{3600}\,\omega t)\ . \qquad (9)$$

The quantity jmaxΔx represents the right-most point on the various grids. The computation of p*u at the lateral boundaries is obtained by a straight-forward application of (4).

Condition (8) effectively imposes a "solid wall" type lateral boundary; however, the experiments are terminated before the wave perturbations reach the wall. At the fine-mesh lateral boundary, we have a harmonic oscillator that determines the pressure for all time at that location. The amplitude of the oscillation is lcb (see Eqn. (9)), and its location insures that perturbations approach the interface of the grids from the fine-mesh sides only. The frequency of the oscillation (ω) determines the wavelength of the perturbation. Table 1 lists wavelengths associated with various gravity-wave oscillator frequencies.

Table 1. Gravity-Wave Oscillator Frequencies and Associated Wavelengths

Frequency* (ω) hr^{-1}	Wavelength (km)	Fine Mesh Intervals (No.)
1	1054.8	35.16
2	527.4	17.58
3	351.6	11.72
4	263.7	8.79
5	210.96	7.03
6	175.8	5.86
7	150.7	5.02
8	131.85	4.4

* The frequency is the number of complete oscillations per hour.

Table 2 outlines the specific gravity-wave experiments discussed in this section.

Table 2. Gravity-Wave (GW) Experiments

Exp.	Grid-mesh ratio	Propagation speed ($m\ sec^{-1}$)	Grid arrangement (fig. 1)	Frequency of oscillation (hr^{-1})	Comments
GW1	3:1	293	1	1	1:1 ratio of time steps
GW2	Do.	Do.	Do.	4	
GW3	Do.	Do.	Do.	Do.	3:1 ratio of time steps

Figure 2 shows the pressure distribution at selected times for experiment GW1. The wave amplitudes and lengths are very nearly conserved throughout the time integration. Therefore, the presence of the mesh interface does not result in serious effects to perturbations with wavelengths of approximately $35\Delta x$ fine-grid intervals. The capability of our mesh refinement technique to deal with relatively long waves agrees with the analytic results obtained by Morse (1973).

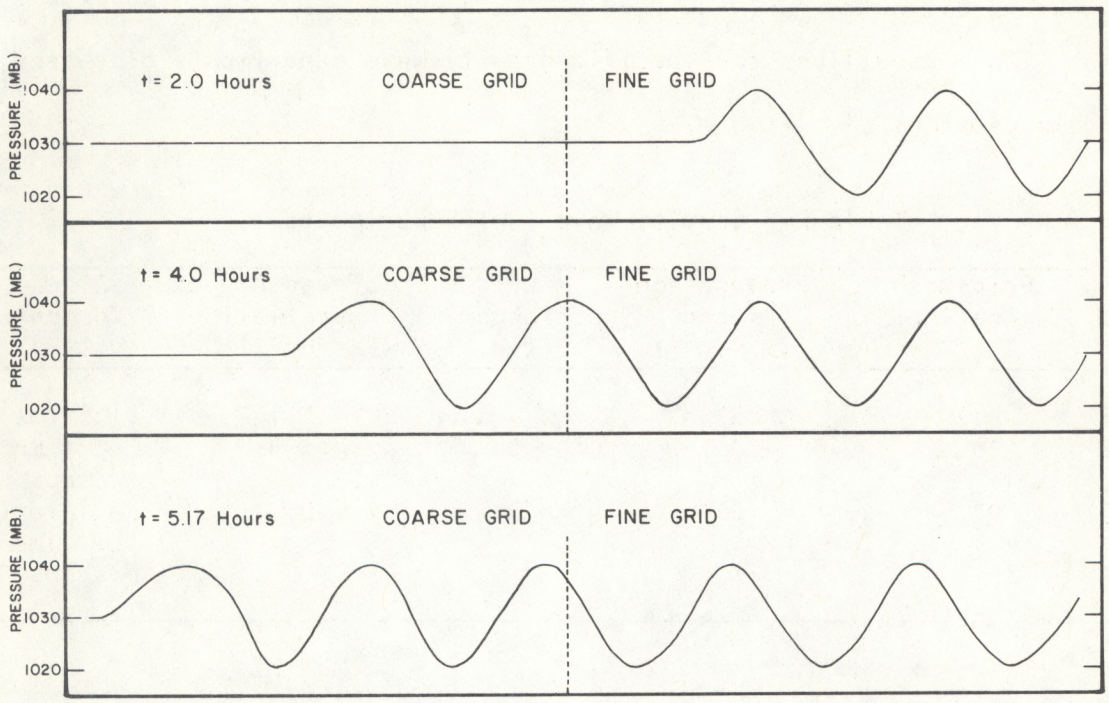

Figure 2. Evolution of pressure profile for experiment GW1. Vertical dashed lines represent the mesh interface.

Figure 3 compares the theoretical ratio of the reflected-to-incident amplitude on the fine mesh (after Morse, 1973) with that obtained numerically. The technique used for approximating the amplitude of reflection in the numerical computations is presented in Appendix A. For the range of wavelengths shown, the numerical and theoretical computations agree reasonably well and show that the magnitude of reflection increases for decreasing wavelengths. The theoretical computations are not valid for wavelength of less than 9.2 fine-mesh intervals. The numerical computations, discussed below, confirm this result.

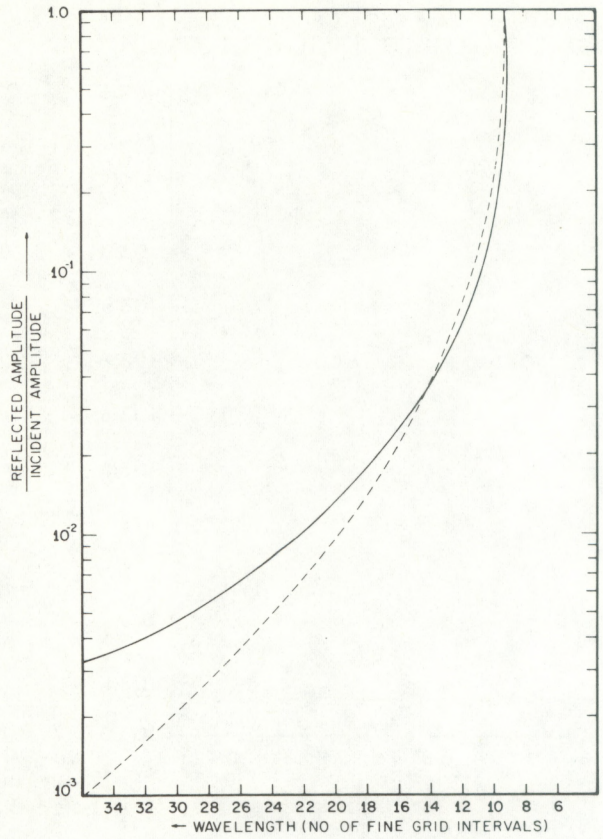

Figure 3. Theoretical (dashed curve) and numerical (solid curve) ratio of reflected to incident amplitudes for gravity wave experiments.

Figure 4 illustrates the numerical absolute maximum, fine-mesh pressure deviation from the incident amplitude as a function of frequency. This deviation is an approximate measure of the reflected amplitude. The frequency $\omega = 2.8\ hr^{-1}$, corresponding to a 9.2 fine-mesh interval wavelength, approximates a "cutoff" frequency, above which the reflected amplitude roughly equals the incident amplitude. Figure 4 also illustrates the maximum coarse-mesh transmitted amplitude as a function of frequency.[1] Up until $\omega = 3.4\ hr^{-1}$

---

[1] In both the amplitude calculations, we have not included the effect of the leading, computationally dispersed perturbation (e.g., the top of fig. 5). These precautions are particularly pertinent in computing the correct amplitudes for the shorter wavelength (higher frequency) perturbations, because the dispersion effects are more pronounced.

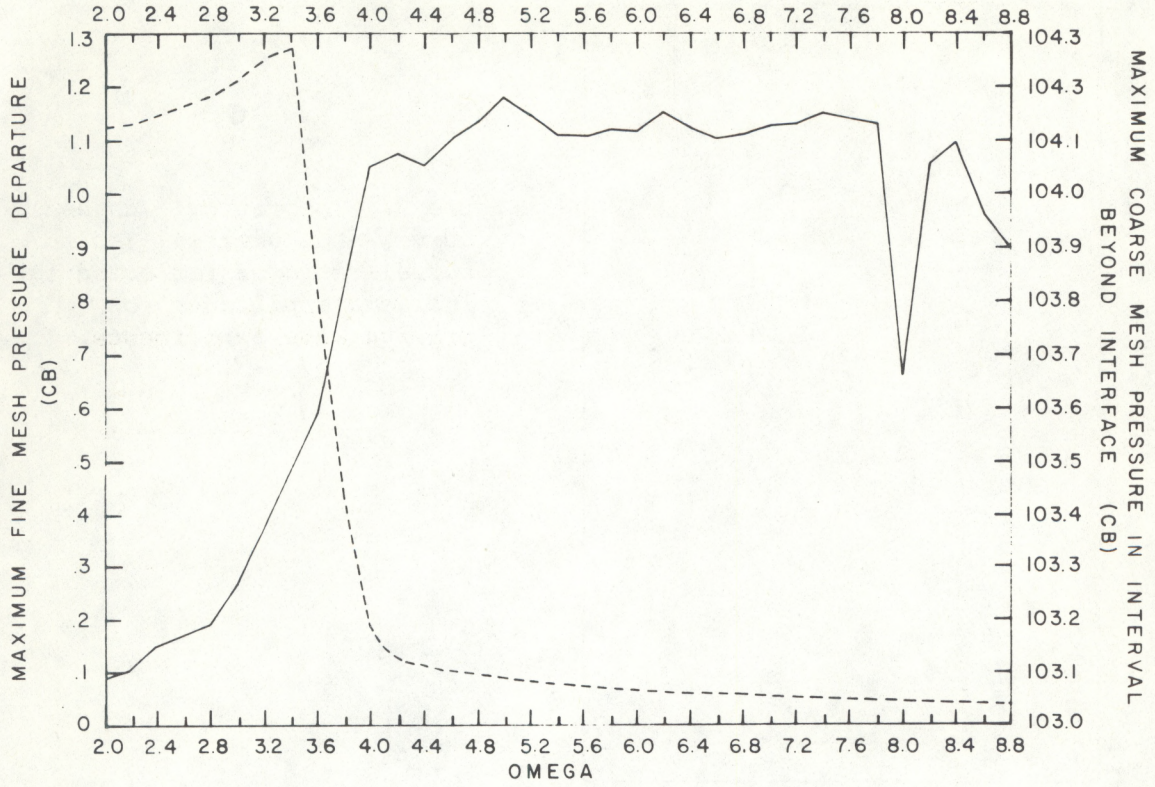

Figure 4. Numerical maximum absolute pressure deviation from incident amplitude (solid curve) and transmitted coarse-mesh pressure (dashed curve) as a function of frequency for gravity wave experiments.

(10.3 fine-mesh intervals), the transmitted amplitude continually increases. Thereafter, the amplitude decreases, and for $\omega = 4$ hr^{-1} it is only 18 percent of the incident value. Thus, the cutoff mentioned above is also manifested by a "trapping" of the wave energy on the fine mesh. Although Morse's (1973) computations only went down to 10.3 fine-mesh intervals, he noted the same inverse relationship between transmitted amplitude and incident wavelength that we also observed up to that point. By showing the evolution of pressure distribution for experiment GW2, figure 5 illustrates how the reflection is manifested on the integration domain. The reflected wave has considerable

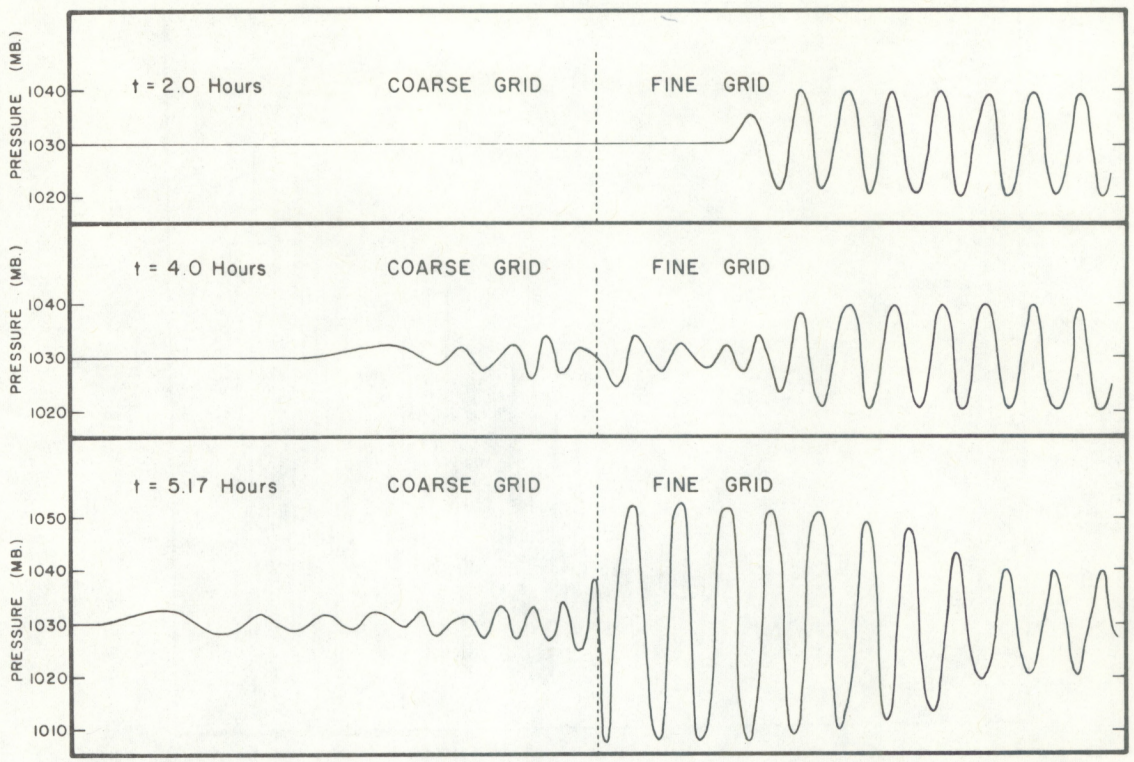

Figure 5. Evolution of pressure profile for experiment GW2. Vertical dashed lines represent the mesh interface.

magnitude, and interacts both constructively and destructively with the incident wave. Also, little energy is transmitted onto the coarse mesh.

Figure 6 compares the evolution of fine-mesh kinetic energy for experiments GW2 and GW3. Experiment GW3 differs from GW2 only in that the coarse-mesh time step is three time greater than that of the fine-mesh. The large amplitude fluctuations after 3.5 hours are a manifestation of reflection. The fluctuations in both these experiments are in phase; however, the amplitude is greater for experiment GW3. Therefore, the use of a longer coarse-mesh time step does not alter the propagation speed of the reflected wave, but it does increase the amplitude of the

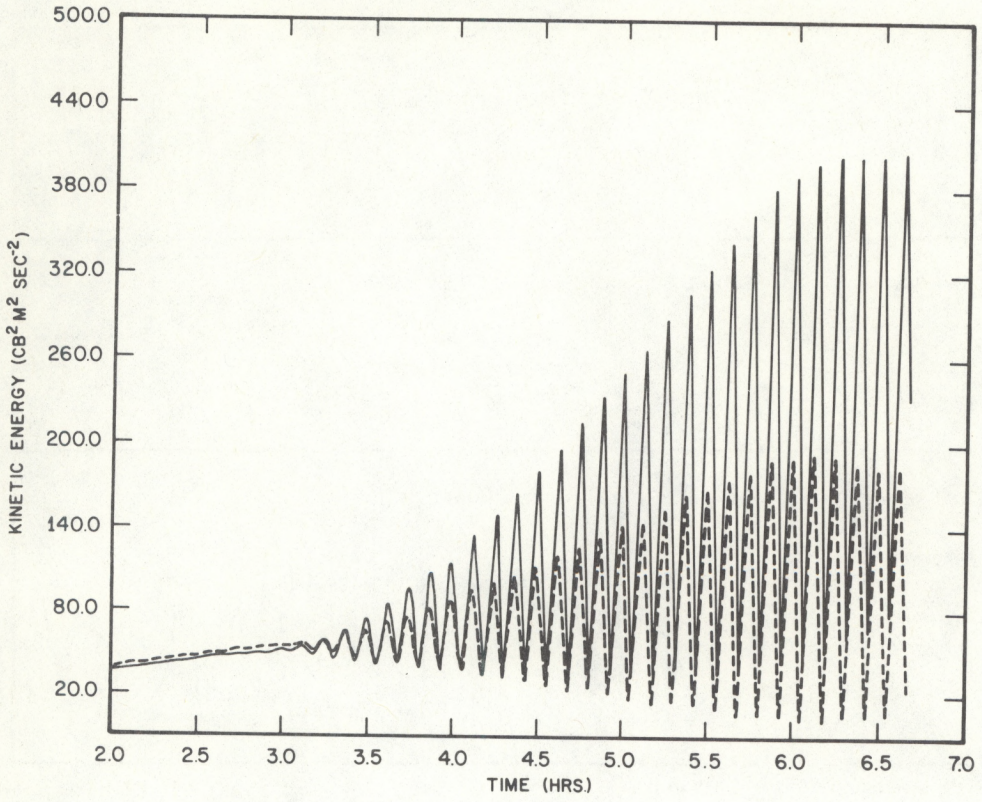

Figure 6. Fine mesh kinetic energy as a function of time for experiments GW2 (dashed curve) and GW3 (solid curve).

reflection. Morse (1973) speculated that a longer coarse-mesh time step would <u>decrease</u> the magnitude of reflection.

4. LINEAR ADVECTION (LA) EXPERIMENTS

The integration procedure used in all but one of the linear advection experiments is the leapfrog scheme given by

$$p^{*n+1}_j = p^{*n-1}_j - \bar{u}\,(p^{*n}_{j+1} - p^{*n}_{j-1})\,\frac{\Delta t}{\Delta x}\,, \qquad (10)$$

which is neutral for $\bar{u}\ \frac{\Delta t}{\Delta x} < 1$. The values of $\bar{u}$ chosen for the experiments presented in this section are -10m sec^{-1} or -300 m sec^{-1}. The initial condition is

$$p^*\ (x,t=0) = \bar{p} \quad , \tag{11}$$

and the lateral boundary conditions are

$$p^*\ (x=0_{coarse},\ t) = \bar{p} \tag{12}$$

and

$$p^*\ (x=jmax\Delta x_{fine},\ t) = \bar{p} + \sin\ (\frac{2\pi}{3600}\ \omega t)\ . \tag{13}$$

The speed $\bar{u}$ = -10 m sec^{-1} is only about 4 percent of the gravity wave propagation speed. Therefore, the frequency of the oscillator must be changed accordingly. If we were to choose ω = 2 hr^{-1}, for example, the perturbation wavelength would be only 0.6Δx fine-mesh grid intervals and could not be resolved on the grids. Table 3 lists the wavelengths associated with various oscillator frequencies for the linear advection experiments with $\bar{u}$ = -10 m sec^{-1}. When the

Table 3. Selected Frequencies and Associated Wavelengths for the Linear Advection Experiments

Frequency (ω) hr^{-1}	Wavelength (km)	Fine Mesh Intervals (No.)
0.0333...	1080	36
0.05	720	24
0.0666...	600	18
0.01	360	12

advecting current is -300 m sec^{-1}, the appropriate frequencies and corresponding wavelengths are essentially the same as those presented in table 1.

Table 4 outlines the specific linear advection experiments discussed in this section.

Table 4. Linear Advection (LA) Experiments

Exp.	Grid-mesh Ratio	Advection Speed (m sec^{-1})	Grid Arrangement (Fig. 1)	Frequency of Oscillation (hr^{-1})	Comments
LA1	3:1	10	3	0.033...	3:1 ratio of time steps
LA2	Do.	Do.	Do.	0.05	Do.
LA3	Do.	Do.	Do.	0.066...	Do.
LA4	2:1	Do.	Do.	Do.	2:1 ratio of time steps
LA5	Do.	Do.	Do.	0.1	Do.
LA6	Do.	Do.	Do.	Do.	Lax-Wendroff integration scheme; 2:1 ratio of time steps
LA7	3:1	300	Do.	4	3:1 ratio of time steps
LA8	Do.	Do.	2	Do.	Do.
LA9	Do.	Do.	Do.	Do.	Upstream differencing for interface tendency; 3:1 ratio of time steps

Figure 7 compares the pressure profiles at 150 hr for experiments LA1, LA2, and LA3. The experiments differ only in the wavelengths of the perturbations. The 36 Δx fine-grid wave (experiment LA1) passes through the interface without any serious alterations in the wave train. The 24 Δx fine-grid wave (experiment LA2) is well represented on the coarse mesh; however, some 2 Δx separation is noticeable in the troughs and ridges on the fine mesh. In experiment LA3, the 2 Δx noise is of greater magnitude than in experiment LA2 and is more widespread; this indicates that the amount of separation varies inversely with wavelength. Also, the transmitted amplitudes are considerably reduced on the coarse mesh.

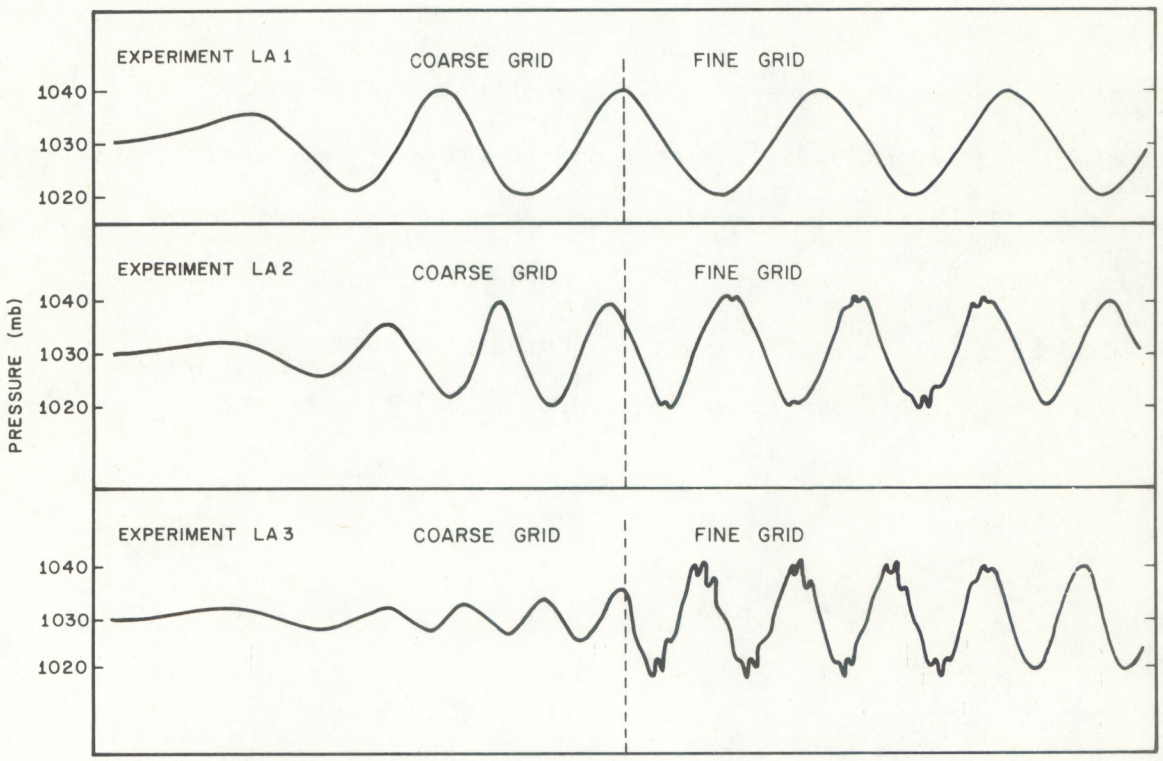

Figure 7. Pressure profiles at 150 hr for experiments LA1, LA2, and LA3. Vertical dashed lines represent the mesh interface.

Browning et al. (1973) used a leapfrog scheme in numerical experiments with a different mesh refinement technique applied to the one-dimensional linear advection equation. They found that perturbation wavelengths $\leq$ 6 Δx coarse-grid intervals could not be transmitted from the fine to the coarse mesh. Although our 6 Δx coarse-grid (18Δx fine grid) waves are not completely void on the coarse mesh in experiment LA3, this wavelength is fairly close to the cutoff discussed below.

Figure 8 portrays the maximum fine-grid and the transmitted coarse-grid pressure as a function of frequency (see ff. 1). The fine-grid noise separation and the trasmitted amplitude increase slightly with decreasing wavelength up until $\omega = 0.05\ hr^{-1}$. After $\omega = 0.05\ hr^{-1}$, however, the separation is more pronounced on the fine grid, and the transmitted waves decrease sharply in amplitude. At $\omega = 0.075\ hr^{-1}$ (a 16Δx fine-grid or 5.33...Δx coarse-grid interval wavelength), the coarse-grid amplitude is only 10 percent of the incident fine-grid value. Therefore, wavelengths in the neighborhood of 16Δx fine-grid intervals may be though of as corresponding to a short-wave cutoff for the linear advection experiments with a 3:1 grid-mesh ratio.

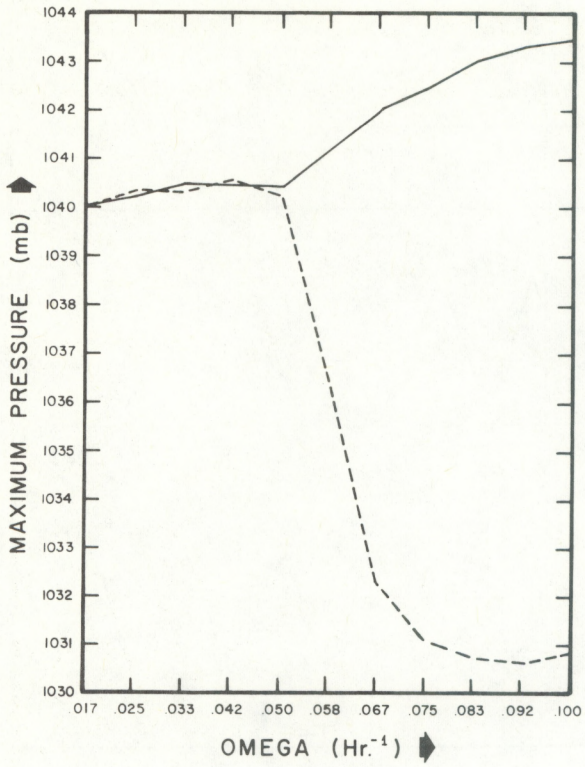

Figure 8. Maximum fine-grid pressure (solid curve) and transmitted pressure (dashed curve) as a function of frequency for linear advection experiments with 3:1 grid mesh ratio.

Figure 9 illustrates the evolution of pressure distribution for experiment LA3. Before the wave reaches the interface (50 hr), the wave train is relatively undisturbed. At 100 hr, some noise appears on the fine mesh near the interface, and by 150 hr it has propagated (at the same speed as the advecting current) well back into the fine mesh. The implication of the above sequence is that the noise is generated at the interface of the grids.

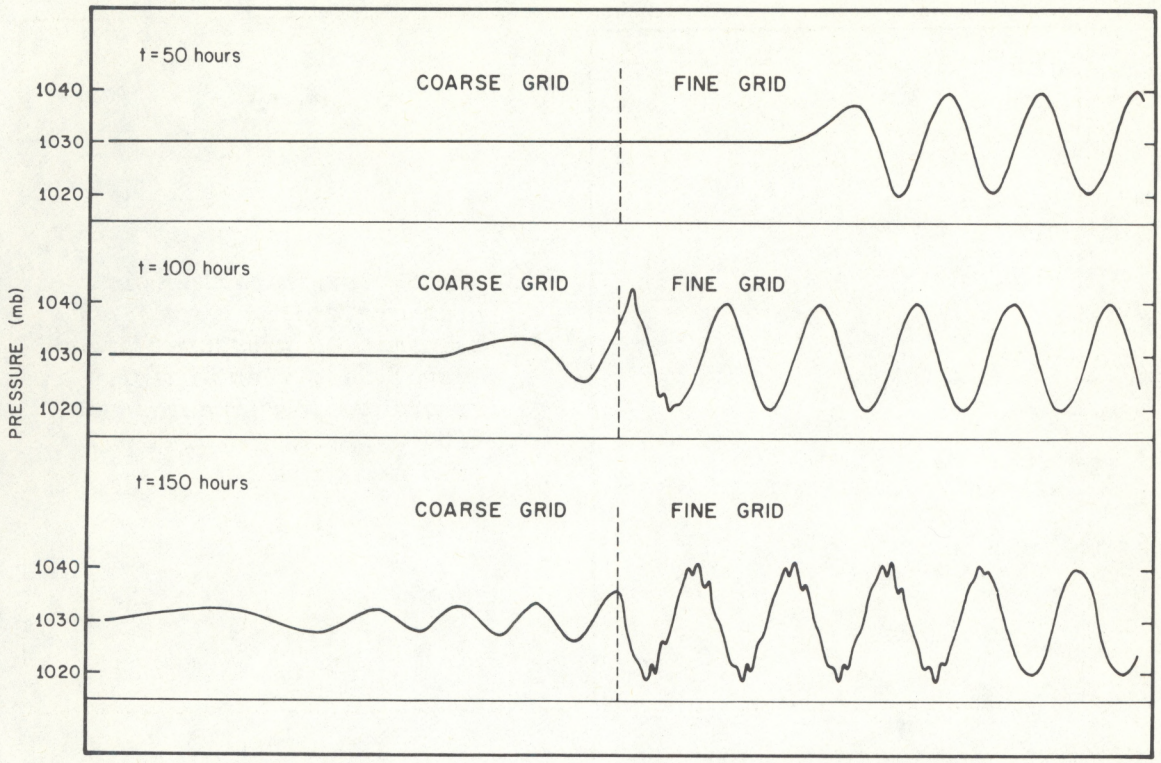

Figure 9. Evolution of pressure profiles for experiment LA3. Vertical dashed lines represent the mesh interface.

Figure 10 compares the pressure distribution at 150 hours for experiments LA4, LA5, and LA6. In these experiments, the grid-mesh ratio is 2:1. The wavelengths of the incident perturbations are the same in experiments LA3 and LA4; however, the fine mesh abberations are not as pronounced with the 2:1 grid-mesh ratio (c.f. the bottom segment of fig. 9). The waves in experiment LA4 are well represented on the coarse mesh. In experiment LA5, the incident perturbation wavelength is smaller than in experiment LA4 and fine mesh noise and coarse mesh amplitude reduction are evident. The results of experiments LA3, LA4,

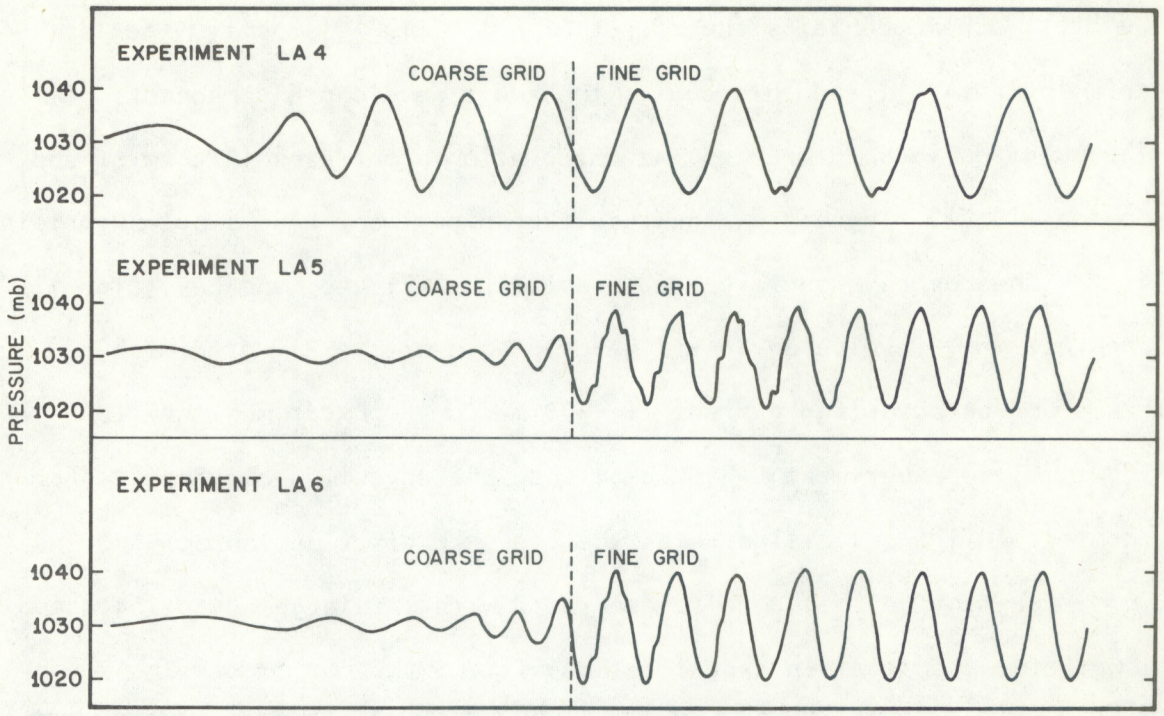

Figure 10. Pressure profiles at 150 hr for experiments LA4, LA5 and LA6. Vertical dashed lines represent the mesh interface.

and LA5 show that the magnitude of the fine-mesh separation and the amount of coarse mesh amplitude reduction are a function of both the incident wavelength and the ratio of the grid increments.

In experiment LA6, the Lax-Wendroff integration procedure given by

$$p^{*n+1}_j = p^{*n}_j - \bar{u}(p^{*n}_{j+1} - p^{*n}_{j-1}) \frac{\Delta t}{2\Delta x} + \frac{1}{2}\bar{u}\left(\frac{\Delta t}{\Delta x}\right)^2 (p^{*n}_{j+1} - 2p^{*n}_j + p^{*n}_{j-1}) \qquad (14)$$

is used; otherwise, this experiment is identical to experiment LA5. Some noise evident near the interface, but it does not encompass as much of the fine grid as is apparent in experiment LA5. The Lax-

Wendroff scheme contains the effect of artificial viscosity (the last term in Eqn. 14), and this causes the short wavelength components of the solution to be damped as the calculation progresses (Richtmyer and Morton, 1967). Therefore, the result of experiment LA6 is not surprising.

The common properties of experiments LA7, LA8, and LA9 (fig. 11) are that they involve an $18\Delta x$ fine-grid wave with a 3:1 grid-mesh ratio and an advecting current of -300 m sec^{-1}. Experiment LA7 is identical to experiment LA3, except that the advecting currents differ. The top of figure 11 illustrates the pressure distribution at 5 hr for experiment LA7. The noise generated with the large advection speed is greater than that in experiment LA3 (c.f., the bottom of fig. 9).

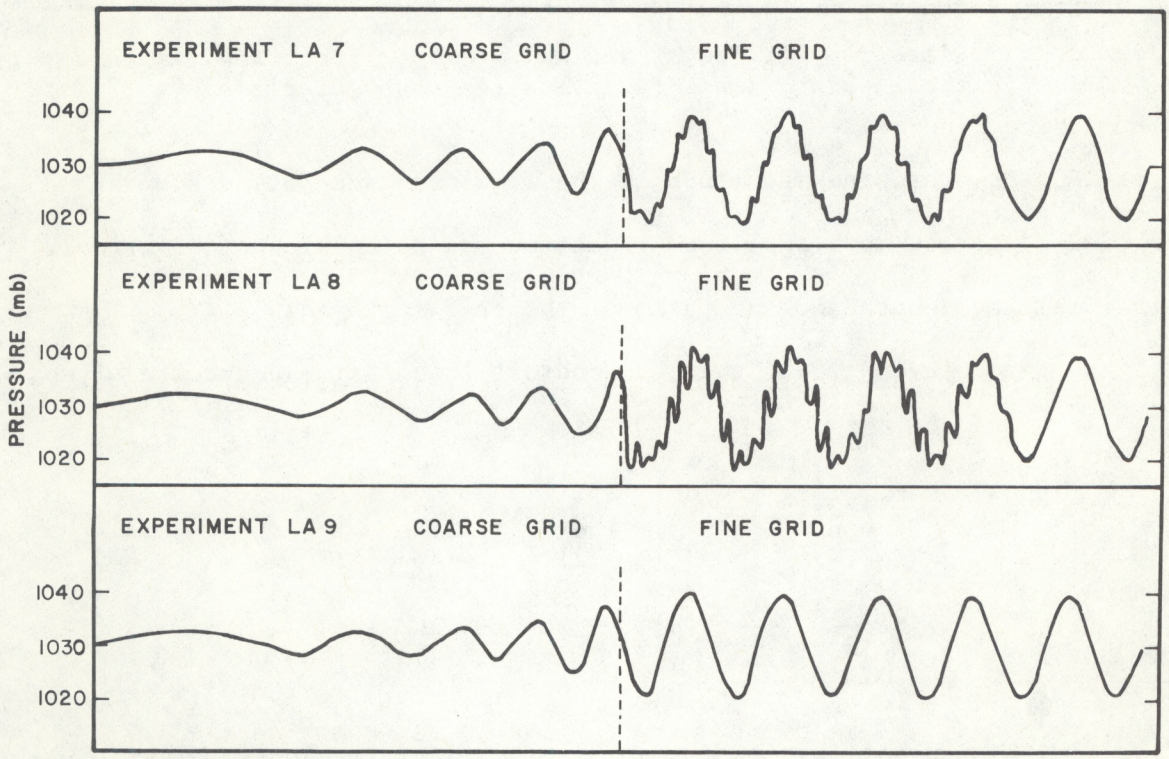

Figure 11. Pressure profiles at 5 hr for experiments LA7, LA8, and LA9. Vertical dashed lines represent the mesh interface.

Experiment LA8 is the same as experiment LA7 except that the computations were performed on grid arrangement 2. This arrangement results in more noise generation than what occurs with grid arrangement 3. That is, averaging the fine-grid interval inside the interface and the coarse-grid tendency just outside the interface (to obtain the interface tendency) gives a better result than does equating the interface tendency to a coinciding coarse-grid value (see fig. 1). In both experiments LA7 and LA8, damping on the coarse grid is apparent.

An explanation for the increased fine-mesh solution separation that occurs in experiment LA8 is that the pressure at the interface is determined entirely from the coarse-mesh, large-scale, forecast. This technique is feasible if the perturbation wavelengths are long, because the fine-mesh wave features are well represented on the coarse mesh. However, the incident perturbation wavelength is short and therefore the coarse grid determined interface pressure lacks sufficient fine-mesh scale structure. The unresolved fine-scale pressure is then reflected from the interface and excites a $2\Delta x$ separation of the solution in the fine-mesh domain.[2] This effect is analogous to that generated by a wave reflected off a solid wall.

---

[2] This argument may be essentially applied to the short-wavelength computations on grid arrangement 3 because the interface tendency is partially determined from the coarse grid computations.

Charney et al. (1950) showed that for a forecast of barotropic vorticity, the boundary vorticity must be specified (independent of the interior solution) on "... that part of the boundary at which the fluid is entering the interior region." In our computations for a wave traveling from the fine to the coarse mesh, the "interior region" may be considered as the coarse mesh and the "boundary" the mesh interface. Therefore, if the interface tendency is determined entirely from the fine mesh, the boundary specification quoted above would be satisfied. This, in combination with the arguments presented in the previous paragraph, forms the basis for experiment LA9.

Experiment LA9 is the same as experiment LA8, except that the interface tendency is computed by upstream differencing where

$$\left(\frac{\partial p^*}{\partial t}\right)_{\text{interface}} = -\bar{u}\left(\frac{p_2^* - p^*_{\text{interface}}}{\Delta x_{\text{fine}}}\right), \qquad (15)$$

and p_2^* is the pressure one fine-grid interval inside the interface. Although the coarse-grid waves are still damped, there is no apparent separation on the fine grid. The effectiveness of this technique in eliminating boundary induced noise, for a limited area fine-mesh forecast of vorticity, was demonstrated by Shapiro and O'Brien (1970).

5. SUMMARY AND CONCLUSIONS

In the gravity wave experiments having a 3:1 grid-mesh ratio, the amplitude of waves reflected and transmitted from the mesh interface slowly increased for decreasing wavelengths down to approximately

10.3Δx fine-grid intervals. These amplitude changes agreed quite well with the theoretical results obtained by Morse (1973). He terminated his computations at 10.3Δx fine-mesh intervals, however, and we performed numerical experiments with smaller incident wavelength perturbations. As the wavelength approached 9.2Δx fine-mesh intervals, the reflected and incident amplitudes became almost equal and the transmitted amplitudes were considerably reduced. Morse (1973) also showed that the aberrations caused by short-wavelength interactions with the mesh interface could be reduced if a smaller grid-mesh ratio was implemented. To a certain extent, we confirmed this result in the linear advection experiments with a 2:1 grid mesh ratio.

Browning et al. (1973) found that wavelengths of approximately 6Δx intervals and below could not be advected on a uniform grid. When the coarse-mesh wavelengths were this small, their numerical nested-grid computations allowed no transmission from the fine mesh onto the coarse mesh. Our linear advection experiments, with a different mesh refinement technique, showed essentially the same phenomenon.

In addition to verifying some of the results of Morse (1973) and Browning et al. (1973), we also demonstrated the following: Using the same time step on both grids reduces the amplitude of gravity wave reflection; and that the 2Δx solution separation that occurs in the short wavelength linear advection experiments can be effectively eliminated by computing the interface tendency with upstream differences.

6. ACKNOWLEDGMENTS

The writer thanks Dr. Robert W. Jones for a number of stimulating discussions on the subject. The manuscript was reviewed by Dr. Robert W. Jones, Dr. Stanley L. Rosenthal, and Walter James Koss.

All numerical computations in this paper were performed at the NOAA CDC 6600 complex, Suitland, Maryland. Access to the computer facility is via a remote terminal located at the National Hurricane Research Laboratory, Miami, Florida.

7. REFERENCES

Browning, G., H. O. Kreiss, and J. Oliger (1973): Mesh refinement. Mathematics of Computation, 27, No. 121, 29-39.

Charney, J. G., R. Fjortoft, and J. von Neumann (1950): Numerical integration of the barotropic vorticity equation. Tellus, 2, No. 4, 237-254.

Jones, R. W. (1974): A nested grid for a three-dimensional model of a tropical cyclone. To be published in the NOAA Technical Memorandum ERL-WMPO Series (U. S. Department of Commerce, National Hurricane Research Laboratory, Miami, Florida.)

Matsuno, T. (1966): Numerical integrations of the primitive equations by a simulated backward difference method. Journal of the Meteorological Society of Japan, Ser. 2, 44, 76-84.

Morse, B. J. (1973): An analytic study of mesh refinement applied to the wave equation (Part I). NOAA Technical Memorandum ERL-WMPO 5, U. S. Department of Commerce, National Hurricane Research Laboratory, Miami, Florida, 1-14.

Moss, M. S. and R. W. Jones (1973): Results from a one-dimensional, nested grid numerical model (Part II). NOAA Technical Memorandum, ERL-WMPO-5, U. S. Department of Commerce, National Hurricane Research Laboratory, Miami, Florida, 15-42.

Richtmyer, R. D. and K. W. Morton (1967): Difference Methods for Initial Value Problems. (John Wiley and Sons, New York) 405 pp.

Schuman, F. G. (1957): Numerical models in weather prediction: II. Smoothing and filtering. Monthly Weather Review, 85, No. 11, 357-361.

Shapiro, M. A. and J. J. O'Brien (1970): Boundary conditions for fine-mesh limited area forecasts. Journal of Applied Meteorology, 9, No. 3, 345-349.

APPENDIX A. TECHNIQUE FOR APPROXIMATING THE REFLECTED AMPLITUDE

Figure A.1 illustrates the maximum fine-mesh pressure, as a function of time, in a region (points 20 to 60) well away from the interface and the harmonic oscillator, for a gravity wave experiment with $\omega = 2hr^{-1}$. The reflected waves do not reach this region until about 3.6 hr, and the pressure fluctuations until then are a manifestation of truncation error. From 3.6 to 5.4 hr, the fluctuations are erratic and of relatively large amplitude. This occurs because the leading, computationally dispersed waves are not monochromatic and, thereby, contain very short wavelength components. These components are easily reflected and have relatively large amplitude. Since we are only concerned with the $17.58\Delta x$ fine-grid interval waves

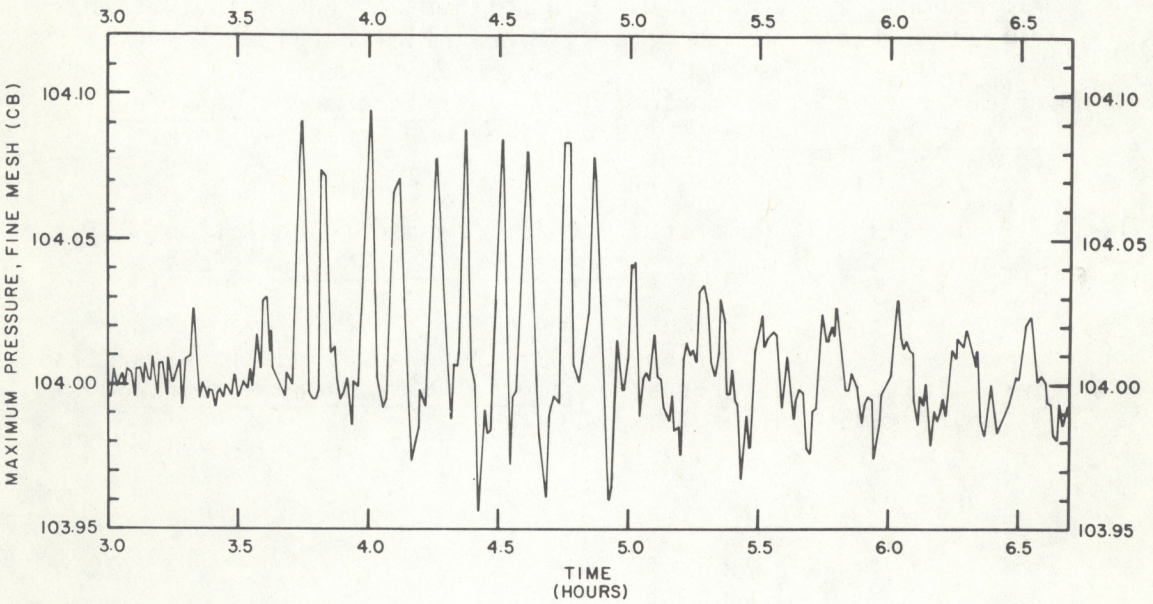

Figure A.1. Evolution of maximum pressure, in a selected region of the fine mesh, for a gravity wave experiment with $\omega = 2\ hr^{-1}$.

(table 2), the pressure values until 5.4 hr are ignored. From 5.4 to 6 hr, the interactions of the reflected and incident wave trains produce the steady oscillation that would be expected for a monochromatic wave. The waves reflect off the fine-mesh oscillator and reenter the region at about 6 hr. Therefore, only the period from 5.4 to 6 hr is used to approximate the amplitude of the wave reflected from the mesh interface.

After determining the appropriate time period to examine, we average the values in the peaks above and below 104 cb (the amplitude of the oscillator is 1 cb). The reflected amplitude is assumed to be equal to the absolute maximum of the deviation averages. The averaging procedure is applied to smooth out the abberations caused by truncation error.